A simple procedure for generating locally refined 2D quadrilateral finite element meshes of gears

Victor Roda-Casanova*, Francisco Sanchez-Marin

Department of Mechanical Engineering and Construction, Universitat Jaume I, Castellon, Spain

Abstract

This article describes a new procedure for automated generation of two-dimensional locally refined quadrilateral meshes of gear drives. In this new procedure, a base mesh is generated using a multiblock meshing procedure. Then, selected elements of the base mesh are subdivided to obtain a refined mesh in certain parts of the gear teeth.

The proposed procedure is completed with a mesh quality enhancement technique, which is based on an optimization-based smoothing. It also includes strategies that allow to automatically identify and refine those areas of the gear that are typically subjected to elevated stress gradients.

The performance of the proposed procedure is illustrated with numerical examples, and it is compared to other existing meshing procedures, both in terms of mesh distortion and accuracy of the results.

Keywords: Gear drives, Finite element analysis, Mesh generation

1. Introduction

Since Wilcox [1] started using it in 1973 to determine the stresses in gear teeth under load, the finite element method has become an essential technology in the research and development of gear transmissions. In the last years, this analysis technique has been used for a wide range of applications, including the determination of the contact and bending stresses of the gears under load [2, 3, 4, 5] and the prediction of the bulk and flash temperatures of the gears in operating conditions [6, 7, 8].

According to Litvin [9], the development of a finite element model of the gear drive can be accomplished by means of three steps. In the first step, a finite element mesh is generated for the gear drive. In the second step, the potential contact surfaces are identified and contact pairs between gear teeth are defined.

*Corresponding author:
Email address: vroda@uji.es (Victor Roda-Casanova)

Finally, in the third step, the boundary and loading conditions under which the analysis is conducted are established.

Let us draw our attention to the first one of these steps, where the gear geometries are generated and then discretized into a set of finite elements. This is an important step in a finite element analysis, as it affects not only its computational cost, but also the accuracy of the obtained results. To build an optimal finite element mesh, two main rules should be fulfilled: first, to obtain results with a high level of accuracy, the finite element mesh must have a high density of elements in those regions of the model where elevated gradients of the studied variables are produced [1, 10]; and second, to shorten the computation time associated to the analysis, the density of the mesh should be reduced in those regions of the model where low gradients are expected. The ability of producing meshes with variable mesh density is usually referred to as local mesh refinement.

Another aspect that must be born in mind during the construction of the finite element mesh is the distortion of its elements [10], because the presence of distorted elements may compromise the accuracy of the results of the finite element analysis [11, 12, 13]. In particular, Coy [14] showed the negative effects that the distorted elements have over the contact results in spur gear transmissions. For these reasons, distorted elements must be avoided, especially in those areas where elevated stress gradients are expected.

Several methods have been developed to discretize a gear geometry into finite elements. Among them, the one proposed by Argyris et al. [15] could be considered one of the most relevant, as there are many authors who have decided to use it in their works [4, 6, 16, 17, 18]. Argyris' procedure offers the advantage of being fast and easy to implement, but it tends to generate distorted elements in regions of the gear tooth where elevated stress gradients are usually produced. In addition, this meshing procedure does not allow the performance of local mesh refinement, as it generates symmetric meshes in both the leading and the trailing sides of the tooth.

In order to produce mesh refinements in certain parts of the gear teeth, some researchers started using structured meshes with specific element arrangements. For example, Li [19] developed finite element models in which the finite element meshes where refined at the fillet and the contact areas. Gonzalez-Perez [20] used a modified version of the Argyris meshing procedure in which some features were incorporated to the finite element models for a better control of the mesh refinement around the contact point.

Although the mesh refinement strategies used in the aforementioned works allowed to increase the mesh density in certain parts of the tooth (and in consequence the accuracy of the analysis), the mesh propagation effect caused the mesh refinement to be not local, but global. This means that refined meshes are obtained in parts of the gear teeth where they are not required, and in consequence, the efficiency of these meshes is reduced and their associated computational time increased. Besides that, keeping structured meshes in the refined areas leads to the appearance of undesired distorted elements [21].

To solve these issues, Mao [2] and Gonzalez-Perez [22, 23] developed mesh-

ing procedures where independent meshes are generated for different parts of the gear tooth, and then they are joined together using multi-point constraints (MPCs). By doing this, meshes with different element density can be obtained for each part of the tooth, thus allowing the performance of local mesh refinement. However, Roarty [24] and Keskin [25] showed that using MPCs to connect non-conforming meshes can produce numerical errors at the mismatching interfaces and introduce difficulties in the generation of the finite element model.

A different approach was presented by Barbieri [21], who introduced the idea of performing adaptive mesh refinement in the finite element meshes of the gears. This adaptive refinement is performed using a commercial finite element solver, where the gear geometries are introduced as non uniform rational B-splines (NURBS). Although this approach has its advantages, it requires of dedicated commercial software and, in addition, generic gear geometries cannot be accurately described using NURBS.

Recently, a procedure to create finite element meshes of gear transmissions was developed by the authors of this work [26]. This procedure has the advantage of allowing the performance of local mesh refinement and, in addition, it reduces the distortion of the elements of the mesh. However, the local mesh refinement capabilities offered by this meshing procedure are limited, as it can only be defined at the surface of the gears, without any control of the behavior of the mesh underneath the surface. Besides that, it generates distorted elements when the size of the elements in the refined area is very small compared with the size of the elements of the base mesh.

In this work, a new meshing procedure to perform the automated generation of quadrilateral meshes over gear sections is proposed. This new procedure is aimed to overcome the limitations of the previously proposed meshing procedure by enhancing its local mesh refinement capabilities, allowing the definition of refinement areas in any part of the domain, without compromising the quality of the resulting mesh.

2. Generation of a base quadrilateral mesh over a gear tooth section

Figure 1 shows a generic tooth section whose geometry is defined by eight boundary curves (representing the left and right fillets, left and right profiles, top land and the parts of the corresponding rim) that are interconnected at points P_i $\{i = 1, 2, ..., 8\}$. Note that points P_3 and P_4 are the frontier between fillet and profile curves. The tooth section is referred to a local coordinate system, whose origin O_L coincides with the center of the gear section. Its Z_L axis is perpendicular to the section plane and the Y_L axis is oriented in such a way that it is centered with respect to the gear section.

In this section a procedure to generate a structured quadrilateral mesh over this generic tooth section is proposed. The development of this procedure is carried out assuming that the parametric equations of the curves that define the geometry of the tooth section are known. The resulting quadrilateral mesh

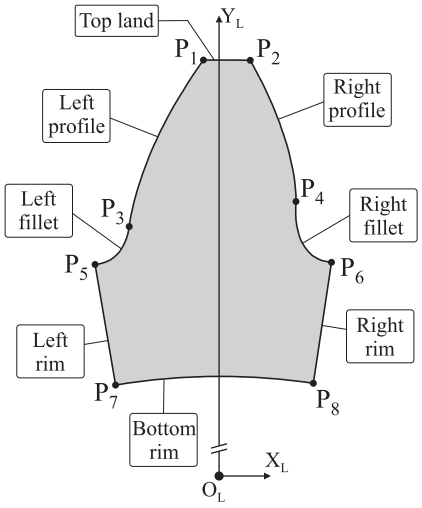

Figure 1: Geometry of a typical gear tooth section

is aimed to serve as a base mesh for the application of the local mesh refinement method described in section 3.

As it can be observed in Fig. 1, a tooth section is a non-convex domain with complex boundaries and, in consequence, generating a mesh over it represents a serious and even intractable problem. To get around these difficulties, researchers [27, 28] recommend using multiblock meshing procedures. The main idea behind these procedures is to decompose the domain into several simpler sub-domains (patches) where a local meshing scheme can be applied. Thus, in the proposed approach, the typical steps of a multiblock meshing procedure are followed to generate a structured quadrilateral mesh over the tooth section:

Step 1. The tooth section is decomposed into simple patches, in such a way that each patch is suitable for the local meshing scheme that will be applied to it. The proposed decomposition is described in section 2.1.

Step 2. Mesh seeds are defined over each one of the boundary curves of the patches. These mesh seeds represent the position that the nodes of the resulting mesh will occupy over them. This step is further discussed in section 2.2.

Step 3. A local meshing scheme is used to generate a quadrilateral mesh over each one of the patches. In this work an algebraic interpolation method based on transfinite interpolation [29] has been selected for such a purpose (described in section 2.3).

Once these steps are concluded, the final mesh is constructed by merging the sub-meshes generated for each patch of the decomposition. In the aim of brevity, the meshing procedure is described for one tooth, since its extension to mesh several adjacent gear teeth is trivial.

2.1. Decomposition of the tooth section in simple patches

There are several aspects that need to be taken into account when choosing a decomposition for the tooth section. Some of them are requirements of the selected meshing scheme, which must be necessarily fulfilled, while others are simple considerations that are made to improve the quality of the resulting mesh.

In this case, the requirement of the selected meshing scheme [29] is that the patches must be bounded by four parametric curves, being topologically equivalent to a square [27]. Besides that, and in order to avoid self-folded and distorted meshes, the patches must be as close as possible to convex regions and the discontinuities in the slope of their boundary curves should be avoided [28]. Furthermore, in order to ease the discretization of the boundary curves and guarantee the continuity of the mesh lines across the boundaries of the patches, the resulting decomposition must be conformal, which implies that any boundary curve cannot be shared by more than two patches.

These requirements and considerations lead us to several ways of decomposing the tooth section, which have been investigated in depth. Among them, the one that proved better results is the one shown in Fig. 2. In this figure, an asymmetric tooth has been selected to explore the most general case, since symmetric teeth are simpler and could be a particular case of asymmetric teeth.

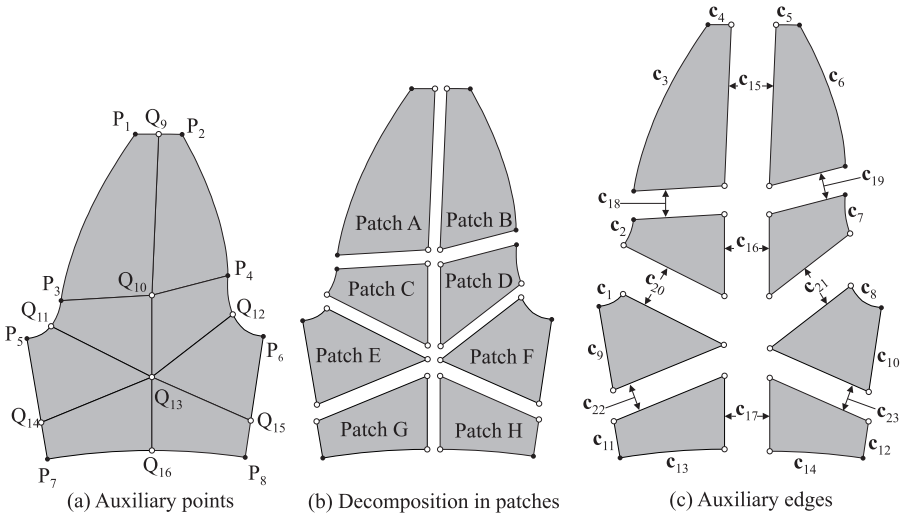

Figure 2: Decomposition of a generic asymmetric tooth section into simpler patches

Starting from the boundary curves of Fig. 1 and their limiting points (P_i), this decomposition is based on the determination of eight auxiliary points, which are denoted by Q_i $\{i = 9, 10, ..., 16\}$ (Fig. 2a). The connections between these auxiliary points and the points P_i allow us to draw lines that divide the tooth section into eight patches (patches A to H in Fig. 2b). To ease the reading of

this work, the boundary curves of the resulting patches are renamed to $\mathbf{c}_i$ $\{i = 1, 2, ..., 23\}$, as indicated in Fig. 2c.

In the proposed procedure, the positions of the auxiliary points Q_i are determined by means of the following steps:

i. Point Q_9 is located at the middle of the top land (Fig. 3a).

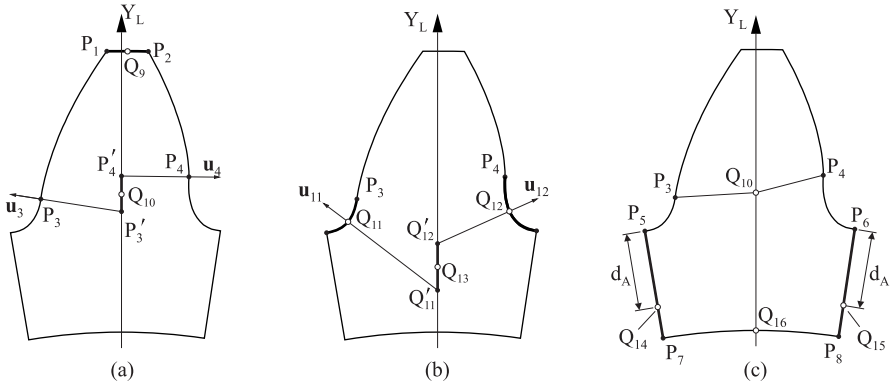

Figure 3: Determination of the position of the auxiliary points in a generic asymmetric tooth section.

ii. Normal vector $\mathbf{u}_3$ at P_3 is determined from the equations of the profile curve. Then, point P'_3 is obtained as the intersection of axis Y_L with the straight line defined by P_3 and $\mathbf{u}_3$. Similarly, P'_4 is obtained from P_4, its associated normal vector $\mathbf{u}_4$ and Y_L. Finally, Q_{10} is determined as the middle point of the segment between P'_3 and P'_4.

iii. Points Q_{11} and Q_{12} are located at the middle point of the left and right fillet curves, respectively (Fig. 3b). At these points, the normal vectors $\mathbf{u}_{11}$ and $\mathbf{u}_{12}$ are determined.

iv. Point Q'_{11} is determined as the intersection of the axis Y_L and the straight line defined by Q_{11} and $\mathbf{u}_{11}$ (Fig. 3b). Similarly, Q'_{12} is determined as the intersection of Y_L and the line defined by Q_{12} and $\mathbf{u}_{12}$. Then, Q_{13} is located at the middle point of the segment between Q'_{11} and Q'_{12}.

v. Distance d_A is defined as the average length of segments $\overline{P_3Q_{10}}$ and $\overline{P_4Q_{10}}$.

vi. Points Q_{14} and Q_{15} are located over the rim sides at a distance d_A from P_5 and P_6, respectively (Fig. 3c).

vii. Finally, point Q_{16} is obtained as the intersection of axis Y_L and the bottom rim boundary curve (Fig. 3c).

When the tooth is symmetric, the procedure becomes simpler because P'_3 and P'_4 are coincident (so is Q_{10}), and this also happens to Q'_{11}, Q'_{12} and Q_{13}.

The resulting decomposition satisfies all the requirements of the local meshing scheme, which are specified at the beginning of this section. In addition, it minimizes the difference in the length of the opposite boundary curves of the patches, which helps improving the aspect ratio of the elements of the resulting

Table 1: General meshing requirements

Requirement	Affected patches	Mathematical condition
R1	F, H	$n_8 = n_{23} = n_{14}$
R2	E, G	$n_1 = n_{22} = n_{13}$
R3	C, D	$n_2 = n_{16} = n_7$
R4	A, C, E	$n_4 = n_{18} = n_{20} = n_9$
R5	B, D, F	$n_5 = n_{19} = n_{21} = n_{10}$
R6	A, B	$n_3 = n_{15} = n_6$
R7	G, H	$n_{11} = n_{17} = n_{12}$

mesh. The proposed decomposition also tries to maximize the orthogonality of the boundary curves at the vertices of the patches, which helps reducing the skewness of the elements of the mesh.

2.2. Specification of mesh seeds along the boundary curves

In this step, a set of $n_i + 1$ mesh seeds is specified over each boundary curve $\mathbf{c}_i$ $\{i = 1, 2, ..., 23\}$ of the tooth decomposition (Fig. 2c). These seeds represent the position that the nodes of the resulting mesh will occupy over the boundary curves, and divide each one of them in n_i segments (or divisions).

The number of divisions in the boundary curves of the patches determines which type of mesh can be generated over them. For example, the generation of a quadrilateral mesh requires the patch to have an even number of divisions in their boundary curves. Moreover, in this particular case a structured quadrilateral mesh is desired, and this requires that the opposite boundary curves of the patches have the same number of divisions. This requirement leads to the seven mathematical conditions shown in Tab. 1, whose fulfillment is mandatory to continue with the meshing process.

Furthermore, the number and the position that the mesh seeds occupy over the boundary curves have a significant impact on the quality of the resulting mesh. In this line, section 3.3 provides some guidelines to distribute these seeds over the boundary curves in order to maximize the quality of the resulting mesh.

2.3. Generation of a quadrilateral mesh over each one of the patches

An algebraic interpolation method based on the transfinite interpolation [29] is selected to mesh the patches in which the tooth section is decomposed. To describe this method, let us consider a generic patch as the one shown in Fig. 4a, which is defined by four boundary curves $\mathbf{c}_i$ $\{i = 1, 2, 3, 4\}$. Over each boundary curve there are distributed $n_i + 1$ mesh seeds that divide it in n_i segments. The requirements described in Tab. 1 cause that the opposite boundary curves of the patch are divided into the same number of segments.

The quadrilateral mesh is generated over this patch following four steps:

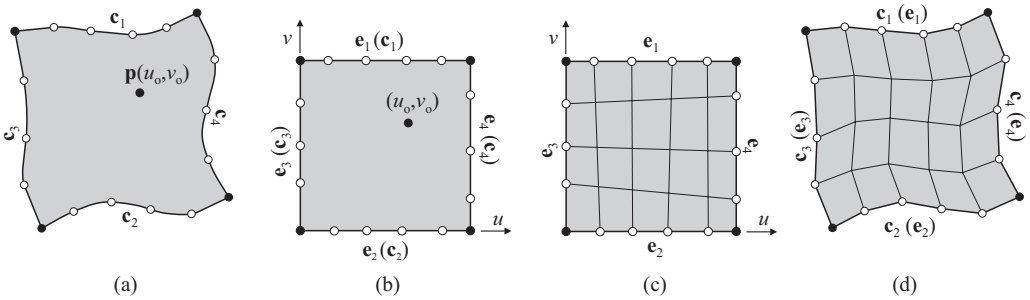

Figure 4: Meshing quadrilateral patches using hierarchical templates

i. The patch is represented in the computational space by a unit square, in such a way that each boundary curve of the patch is logically equivalent to an edge of the unit square $\mathbf{e}_i$ $\{i = 1, 2, 3, 4\}$, as shown in Fig. 4b.
ii. The mesh seeds are transferred from the boundary curves of the patch to the edges of the unit square.
iii. A structured quadrilateral mesh is generated over the unit square using a bilinear interpolation of the transferred mesh seeds (Fig. 4c).
iv. The mesh is mapped from the unit square in the computational domain to the patch using transfinite interpolation [30] (Fig. 4d)

3. Performing local mesh refinement

This section describes a procedure to perform local mesh refinement over a base quadrilateral mesh of a gear section, which may consist of one or more teeth. This procedure is developed under the assumption that the base mesh is generated following the instructions given in section 2, and it consists of two main steps. In the first step (section 3.1), selected elements of the base mesh are recursively subdivided until a certain level of refinement is achieved. The element subdivision causes the appearance of hanging nodes (i.e. nodes that appear in the edges of adjacent elements with different refinement levels), which are removed in the second step of the procedure (section 3.2). In section 3.3, some recommendations for the application of the local mesh refinement are given. Finally, the automatization of the mesh refinement is discussed in section 3.4.

3.1. Element subdivision

The proposed mesh refinement procedure is based on the recursive subdivision of the elements of the base mesh. The parts of the domain that are to be refined are selected using refinement areas, which are defined by a closed polygon, as illustrated in Fig. 5a. A maximum element size is associated to each refinement area, in such a way that when the refinement process is completed, these areas are covered by elements whose size is smaller than the maximum element size specified for each refinement area.

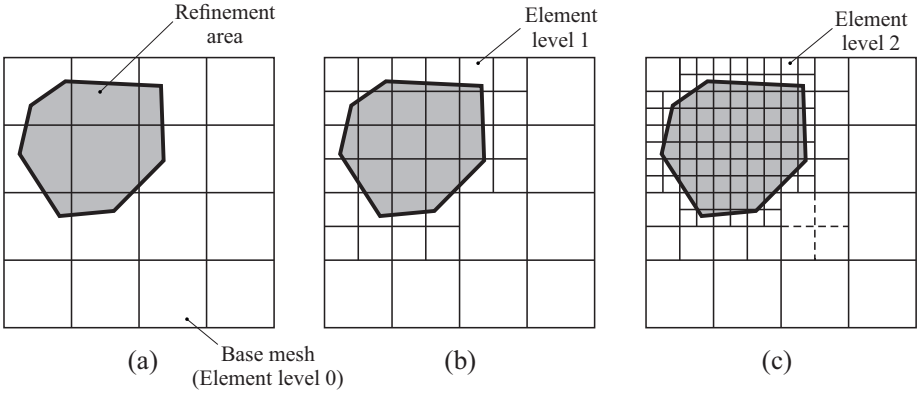

Figure 5: Mesh subdivision process

The element subdivision process is similar to the one followed in a quadtree structure [31]. All the elements of the mesh are checked in turn, and they are divided into four sons when the following conditions are simultaneously fulfilled:

- The area of the element coincides (totally or partially) with a refinement area.
- The size of the element exceeds the maximum element size specified for the particular area.

The process is repeated until no element in the mesh satisfies both conditions. All the element splitting operations are performed in the logical space. By doing so it is ensured that no further adjustments will be required in the position of the nodes in the physical space to match the geometry of the gear tooth.

Each element of the mesh has an associated level number, which represents the number of subdivisions that are required to reach this particular element from an element in the base mesh. The level of the elements of the base mesh is 0, and each time an element is divided, the level of its sons is increased by one. Note that the level of an element can be used to define its relative size with respect to its ancestor in the base mesh. For this reason, the level of the elements is used to define the maximum element size in a refinement area.

After completing the mesh subdivision, a further operation is conducted to ensure that the resulting mesh is strongly-balanced. A strongly-balanced mesh is one where the level difference between any two neighboring elements is either 0 or 1. If this condition is violated, the element with a lower level is divided until that condition is fulfilled. Figure 5c shows an example (in dashed line) of an element that is split to achieve a strongly-balanced mesh. A stongly-balanced mesh is required in order to remove the hanging nodes that arise as a consequence of the mesh subdivision.

3.2. Removing hanging nodes

The element subdivision process described before produces elements with hanging nodes. These hanging nodes produce connectivity issues in the mesh that can cause problems during the finite element analysis, so they need to be removed. Following up the example shown in the previous section, Fig. 6a shows the hanging nodes resulting from the mesh subdivision illustrated in Fig. 5.

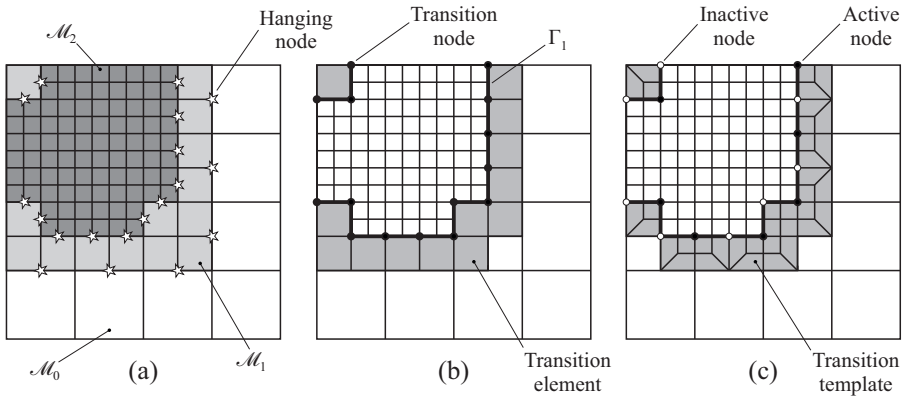

Figure 6: Removing hanging nodes in Γ_2.

Let us define a sub-mesh $\mathscr{M}_i$ as the union of all the elements of a givel level i. Two sub-meshes $\mathscr{M}_i$ and $\mathscr{M}_{i+1}$ intersect along a polyline Γ_i, which can be non-manifold and may consist of disconnected polylines. All those elements in $\mathscr{M}_i$ that contain a node in Γ_i are defined as *transition elements*, and all those nodes of the transition elements that lie on Γ_i are defined as *transition nodes*. Figure 6a shows the three sub-meshes $\mathscr{M}_i$ $\{i = 0, 1, 2\}$ that arise from the mesh subdivision illustrated in Fig. 5. Figure 6b shows the polyline Γ_1, which defines the border between sub-meshes $\mathscr{M}_1$ and $\mathscr{M}_2$ and includes all the transition nodes of the transition elements in $\mathscr{M}_1$.

In order to remove the hanging nodes in the mesh, the 2-refinement strategy proposed by Schneiders [32] is used. This strategy consists in dividing the transition elements using the templates shown in Fig. 7, which establish connections between the hanging nodes and the rest of the nodes of the mesh.

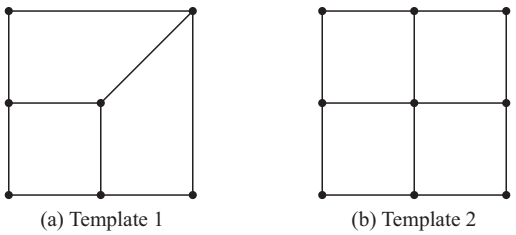

Figure 7: 2-refinement templates for quadrilateral meshes

In the process of removing the hanging nodes, one frontier Γ_i is dealt at a time. Initially all the transition nodes in Γ_i are considered active, and then they are alternatively deactivated, as shown in Fig. 6c. Then, all the transition elements that contain one active transition node are divided using template 1 (Fig. 7a), and the transition elements that contain two or more active transitions nodes are divided using template 2 (Fig. 7b). Note that template 1 is oriented based on the relative location of the active node. This process is repeated for all the frontiers Γ_i between meshes, and the hanging nodes are sequentially removed.

3.3. Guidelines for the application of the mesh refinement

As it has been said before, the proposed mesh refinement strategy is based on the recursive subdivision of the elements of the base mesh. This refinement strategy implies that the quality (in terms of element distortion) of the elements of the refined mesh is highly conditioned by the quality of the elements of the base mesh.

When the base mesh is generated using the procedure described in section 2, its quality is controlled by the number and the position of the mesh seeds over the boundary curves of the patches. This fact is illustrated in Fig. 8a and 8b, where the effect of using two different seeding schemes to mesh the same gear tooth is shown. It can be observed that the elements of the base mesh in Fig. 8a have a poorer aspect ratio than the elements of the base mesh in Fig. 8b.

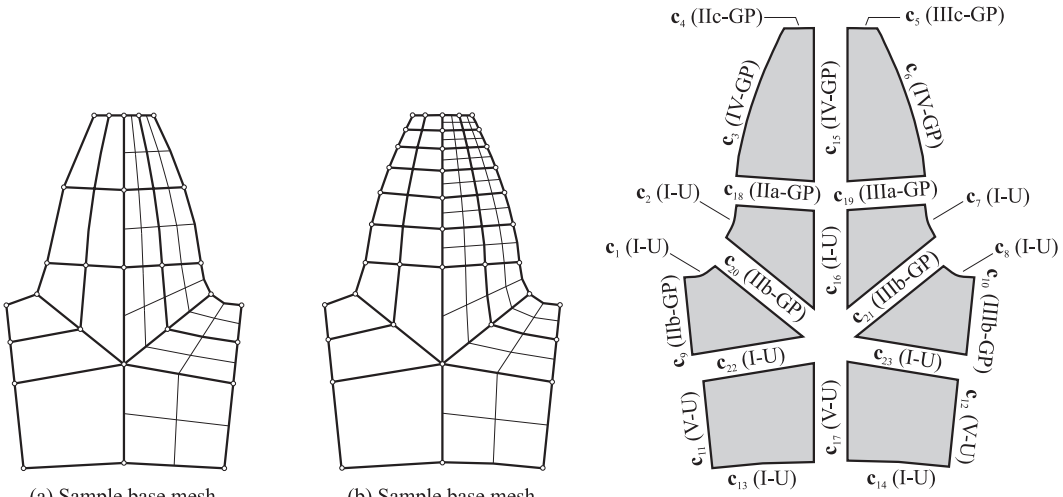

Figure 8: Guidelines for mesh refinement

The elements of the base meshes in Fig. 8a and 8b are subdivided, in order to produce a refined mesh in the right part of the tooth. As it can be observed, the distortion of the elements of the base mesh is propagated through the refined

elements, which evidences the importance of constructing a good quality base mesh in order to increase the quality of the refined mesh.

In order to obtain a high quality final mesh, it is interesting to have a seeding scheme that maximizes the quality of the base mesh and automatizes the mesh generation process. After some investigations related to this matter, the following seeding scheme is proposed:

1. Operation I-U: curves $\mathbf{c}_8$, $\mathbf{c}_{23}$ and $\mathbf{c}_{14}$ are divided into n_{seg} segments of equal length (fulfilling restriction R1 of Tab. 1, Fig. 8c). Then, the same division is performed on curves $\mathbf{c}_1$, $\mathbf{c}_{22}$ and $\mathbf{c}_3$ (fulfilling restriction R2) and on curves $\mathbf{c}_2$, $\mathbf{c}_{16}$ and $\mathbf{c}_7$ (fulfilling restriction R3).
2. Operation IIa-GP: starting from the length of $\mathbf{c}_{18}$ and the length of the adjacent elements of $\mathbf{c}_2$ and $\mathbf{c}_{16}$ (obtained in operation I-U), the parameters of a geometric progression (number of elements, n_{II}, and progression ratio r_{II}) are computed to distribute elements along $\mathbf{c}_{18}$ growing from size of $\mathbf{c}_2$ to size of $\mathbf{c}_{16}$. The resulting number of elements (n_{II}) is rounded to the nearest integer.
3. Operation IIb-GP: starting from the length of the curve, the smallest adjacent element (from all adjacent curves) and the number n_{II} obtained in operation IIa-GP, the progression ratio and the size of all elements are computed for a geometric progression to distribute elements along curves $\mathbf{c}_9$ and $\mathbf{c}_{20}$.
4. Operation IIc-GP: starting from the length of $\mathbf{c}_4$, the numbers of elements n_{II} and the progression ratio r_{II} are used to distribute elements along $\mathbf{c}_4$ in a geometric progression.
5. Operation IIIa-GP: similar to operation IIa, but applied to curve $\mathbf{c}_{19}$ and obtaining parameters n_{III} and r_{III}.
6. Operation IIIb-GP: similar to operation IIb, but applied to curves $\mathbf{c}_{21}$ and $\mathbf{c}_{10}$.
7. Operation IIIc-GP: similar to operation IIc, but applied to curve $\mathbf{c}_5$.
8. Operation IV-GP: considering the length of the curve, and the length of the adjacent elements (of adjacent curves), the parameters of a geometric progression (number of elements and progression ratio) are computed on curves $\mathbf{c}_3$ and $\mathbf{c}_6$. Then, an average number of elements is considered, which is rounded to the nearest integer. With this number of elements, geometric progressions are computed to distribute elements on curves $\mathbf{c}_3$, $\mathbf{c}_{15}$ and $\mathbf{c}_6$.
9. Operation V-U: finally, considering the size of the adjacent elements, curves $\mathbf{c}_{11}$, $\mathbf{c}_{17}$ and $\mathbf{c}_{12}$ are uniformly divided by the same number of elements.

Note that this seeding scheme is fully parametrized through the number of divisions n_{seg} in the boundary curves involved in meshing requirements R1, R2 and R3.

The shape of the elements of the base mesh is not the only source of distorted elements in the refined meshes. Figure 6c shows that, even in the best of the

cases in which all the elements of the base mesh are perfectly squared, elements with skewed angles will arise when template 1 (Fig. 7a) is used to remove the hanging nodes that appear during the subdivision of the elements of the mesh. The appearance of these distorted elements is unavoidable, as they are required in the transition from a coarse to a fine mesh. For this reason, it is strongly recommended to perform a mesh optimization (see section 4) once the mesh refinement process is completed.

3.4. Automatization of the mesh refinement for stress analysis

Once the refinement approach has been defined, the next step is to decide which regions of the domain are candidates for refining. In the case of a stress analysis, refinement of the local mesh is required in those areas of the domain that are subjected to elevated stress gradients. And in gear transmissions, it is known that these areas are usually those affected by the tooth contact and bending stresses. Thus, the mesh refinement process could be automatized by detecting those points where the stresses reach their maximum value and refining the areas that surround them.

On the one hand, the stresses derived from the bearing contact arise in the vicinity of the contact area, and they usually reach their maximum value near the spot where the initial point of contact (Q in Fig. 9a) is produced [33]. This initial point of contact can be easily determined by means of an unloaded tooth contact analysis of the transmission.

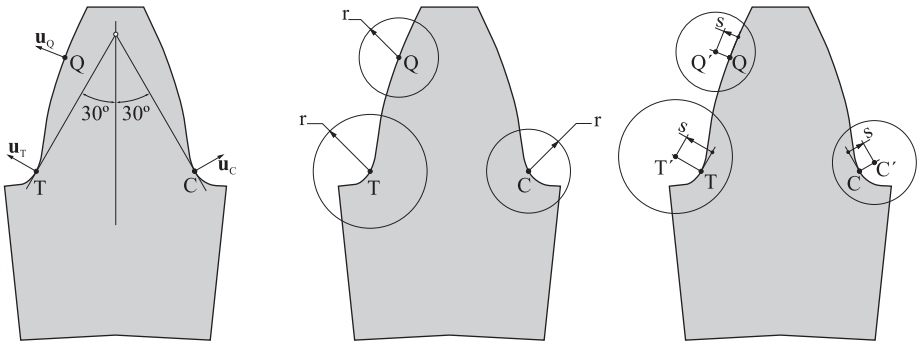

(a) Theoretical location of stress peaks

(b) Definition of the refinement areas

(c) Offset of the refinement areas

Figure 9: Guidelines for automated mesh refinement

On the other hand, bending stresses are produced in the vicinity of the tooth fillets. Although it is not easy to perform an accurate prediction of the points where these stresses reach their maximum values, a quick estimation can be made following the ideas presented in ISO 6336 standard [34]. In this standard, maximum bending stresses are located at the points where straight lines which make an angle of 30° with the local Y_L axis are tangential to the fillet curve (points T and C in Fig. 9a).

After the points P, T and C are located, refinement areas are defined around them. There are many ways to perform this but, in this work and in the aim of simplicity, these refinement areas are defined as circles characterized by their center and radius r. The center of these circles may coincide with the points of maximum stress (Fig. 9b), or it may be displaced a distance s along the boundary curve normal direction, as indicated in Fig. 9c. Note that the radius r and the offset distance s could be different for each refinement area, and could also be positive (outside displacement) or negative (inside displacement).

As it is observed in Fig. 6, the proposed refinement strategy produces abrupt changes between the size of the elements of the base mesh and the elements of the refined mesh. In some cases, this abrupt transition can produce negative effects over the accuracy of the solution of the finite element model, causing local disturbances in the stress field [35]. For this reason, it is interesting to specify smooth transitions between coarse and refined meshes. To do so, overlapped refinement areas can be defined, with a progressive increase of the level of refinement, as shown in Fig. 11b.

For a specific position of the gear transmission, the parametric generation of the tooth geometry, the tooth contact analysis to determine the point of contact, the mesh generation and refinement algorithm, the optimization of the mesh (described in section 4) and the automation of the mesh refinement according to the rules explained in this section have been implemented in a stand-alone application with a graphic user interface, by using MS Visual Studio and C# as programming language. The output of this application is an input file for the Abaqus FEM solver including all the required information of the finite element model.

4. Mesh quality and optimization

It is well known that the presence of distorted elements in the mesh reduces both the convergence rate and the accuracy of the finite element analyses [11, 12, 13]. Unfortunately, automatic finite element mesh generation procedures (as the one presented in this work) cannot avoid the appearance of undesired distorted elements [36] and, for this reason, they are usually completed with mesh improving techniques.

These techniques are aimed to reduce the distortion of the elements once the mesh is generated, and they have been developed under several points of view, giving place to a big number of different methods which Park [37] classified in three groups: adaptivity, smoothing and swapping. In particular, in mesh smoothing the inner nodes of the mesh are moved to an optimum position, in such a way that the distortion of its elements is reduced. Traditionally, mesh smoothing methods have been classified into Laplacian [38] and optimization-based methods. Although the former are more suitable in terms of computational cost, the latter lead to better quality meshes.

In the optimization-based smoothing, the optimum position of the inner nodes of the mesh is determined by solving local or global optimization problems. In these optimization problems, the objective functions are usually re-

lated to mesh quality metrics, which measure the degree of distortion of the elements of the mesh. There is a wide range of mesh metrics that can serve as objective functions in optimization-based smoothing. Among them, the mesh metric proposed by Oddy [39] has proven to be effective in mesh optimization approaches [40].

The mesh quality metric developed by Oddy (f_O) manages to account for element distortions produced by combinations of shearing and stretching effects. In addition, it is independent of the element size and it is not affected by rigid body motions. Its value is zero when the element is undistorted (i.e. it is a square), and it grows to infinity as the distortion of the element increases.

Oddy's metric is calculated for every element of the mesh using the equation presented in Ref. [39]. Then, the quality of a group of elements can be assessed through the average ($f_{O,avg}$) and the maximum value ($f_{O,max}$) of f_O calculated for the elements in that group.

As it has been said before, the optimization can be performed from a local or a global point of view. Although the global approach [41] has proven interesting for meshes with a small number of nodes, it is impractical for meshes containing a large number of nodes [36]. For this reason, the local optimization approach [40] is preferred in this work.

In the local approach the position of each interior node of the mesh is optimized separately. The objective function for the optimization problem is $f_{O,avg}$, which is evaluated considering all the elements that are connected to the node whose position is optimized. In this case, the objective function is a function of the coordinates of the target node, which are given by the position vector $\mathbf{x}_i$. Following the ideas presented by Knupp [40], the local optimization is performed using a modified Newton scheme:

$$\mathbf{x}_{i+1} = \mathbf{x}_i - H(\mathbf{x}_i)^{-1} \cdot G(\mathbf{x}_i) \tag{1}$$

where $\mathbf{x}_{i+1}$ is the optimized position of the node, and G and H are the gradient and the Hessian matrix of the objective function, respectively. The local optimization is performed for each interior node of the mesh, and the global process is repeated until a certain stopping condition is reached. More details about this process can be found in Ref. [40].

5. Numerical examples and discussion of results

The performance of the proposed procedure is illustrated through the development and analysis of a finite element model of a spur gear transmission (denoted as **Proposed** model). The transmission selected for this example consist of two identical standard spur gears, whose geometry is defined by the design parameters included in Tab. 2. The material parameters and operating conditions of the transmission are also shown in Tab. 2.

A typical finite element model of a gear transmission (Fig. 10) is composed by the geometries of the drive and the driven gears, which may consist of one or several teeth. A rigid edge is defined around the rim of each gear geometry, and

Table 2: Parameters of the transmission

	Parameter	Value
Gear design parameters (both gears)	Module	2 mm
	Pressure angle	20 deg
	Addendum of standard basic rack tooth	2 mm
	Dedendum of standard basic rack tooth	2.5 mm
	Fillet radius of the basic rack	0.5 mm
	Tooth number	30
	Facewidth	20 mm
Material parameters	Elastic modulus	210 GPa
	Poisson's coefficient	0.3
Operating conditions	Nominal torque	120 Nm
	Center distance	60 mm

it is rigidly connected to a reference node coincident with the center of rotation of the gear. These reference nodes, which are denoted by O_1 and O_2, are used to specify the boundary conditions of the finite element model.

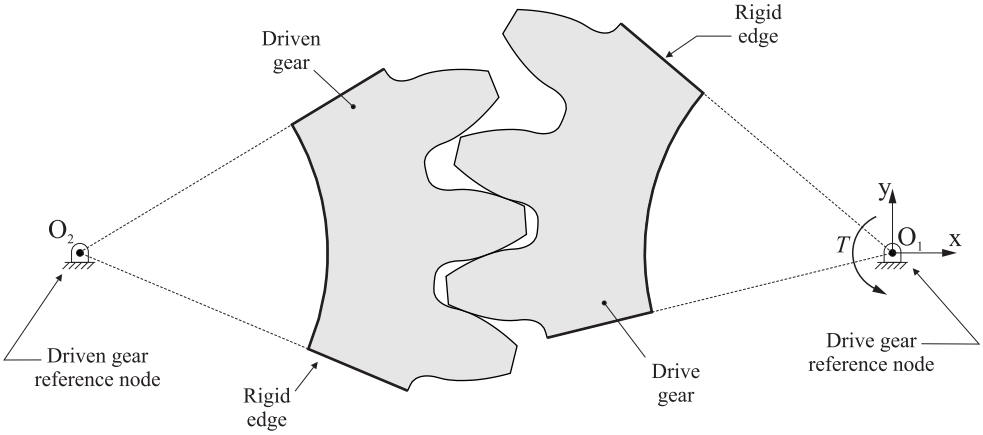

Figure 10: Typical finite element model of a generic gear transmission

Displacements along x and y directions are restricted at reference nodes O_1 and O_2. Rotation around z direction is allowed at node O_1, where a nominal torque T is applied. In contrast, rotation around z direction is prescribed with a certain magnitude at the reference node O_2, which restricts the rotation of the system. The finite element analysis is performed under plane strain hypotheses, in which a linear elastic behavior is assumed for both drive and driven gears.

The gear geometries are generated and then discretized into finite elements using the proposed procedure. The mesh generation process for a gear geometry consisting of a single tooth is illustrated in Fig. 6. In this example, it is assumed

Table 3: Definition of mesh refinement areas

Refinement area	Base point	Offset s	Radius r	Level of refinement
RA1	Q	0.0 mm	0.5 mm	3
RA2	Q	0.0 mm	0.9 mm	2
RA3	T	0.2 mm	0.5 mm	3
RA4	T	0.2 mm	1.0 mm	2
RA5	C	0.2 mm	0.5 mm	3
RA6	C	0.2 mm	1.0 mm	2

that the contact with the mating gear is produced at the pitch point. First, a base mesh is generated over the gear geometry using the procedure described in section 2. The seeding scheme described in section 3.3 has been followed to define the density of the base mesh, selecting $n_{seg} = 2$. As a result, the base mesh shown in Fig. 11a is obtained, which consist of 136 elements and 165 nodes.

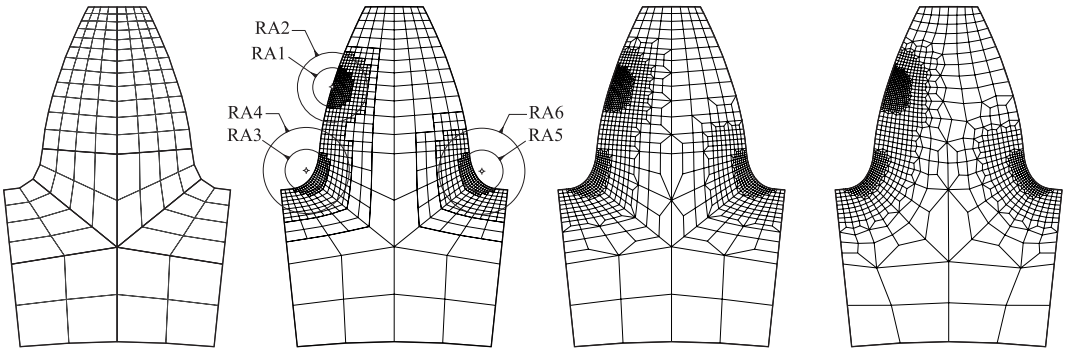

Figure 11: Mesh generation process

After the base mesh is generated, the ideas described in section 3.4 are followed to perform an automated element subdivision that will turn into a localized mesh refinement. As it can be observed in Fig. 11b, six refinement areas are specified (denoted as RA1, RA2, etc.), which are defined by the parameters shown in Tab. 3. To produce a smooth transition between the refined and the base mesh, two concentric refinement areas are defined around each point of maximum stress, with progressive levels of refinement specified for each one of them.

After the elements of the base mesh are subdivided, the hanging nodes that arise during the element subdivision process are removed as explained in section 3.2, giving place to the mesh shown in Fig. 11c. In the process of removing the hanging nodes, 197 new elements and 250 new nodes are created.

Finally, the mesh smoothing technique described in section 4 is applied to reduce the distortion of the elements of the mesh and, as a result, the final mesh shown in Fig. 11d is obtained. For the optimization process, 10 iterations of the mesh smoother have been considered. The number of nodes and elements in the mesh is not affected by mesh smoothing, because this technique does not change neither the connectivity nor the number of nodes of the discretization.

Following these ideas, the geometries of the drive and the driven gears are independently meshed and then included into the finite element model of the gear transmission. It must be pointed out that finite element models in which the gear geometries consist of a single tooth are seldom used, because they do not allow to obtain a realistic load sharing distribution between teeth when simultaneous contacts are produced. In addition, the presence of rigid edges near stressed areas may introduce inaccuracies in the solution of the finite element model. For these reasons, gear geometries including three or more teeth are typically used in the finite element models, as the one shown in Fig. 12a.

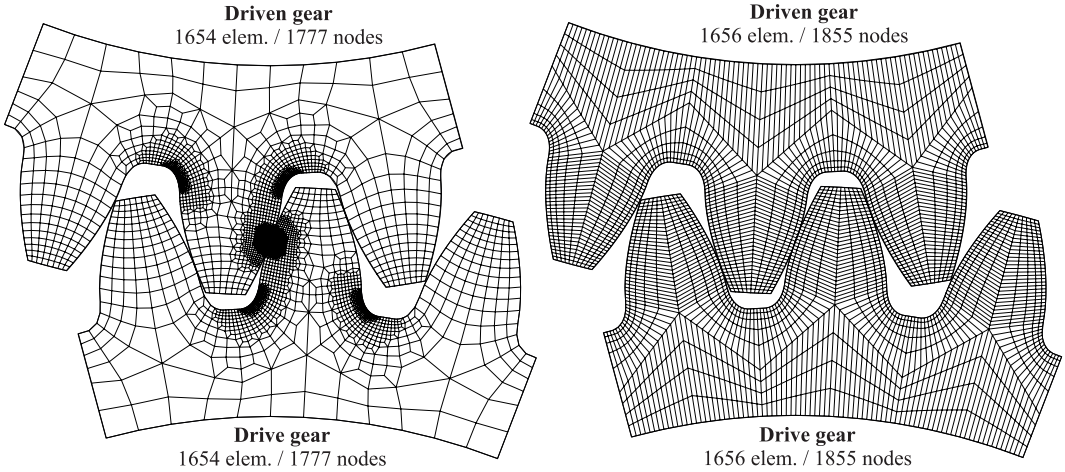

Figure 12: Discretization of the gear geometries

The mesh shown in Fig. 12a has been generated following the same steps as in Fig. 11, considering the refinement parameters shown in Tab. 3. As the drive and driven gears have the same geometry and the contact between them is produced at the pitch point, the meshes generated for both gear geometries are identical. Each one of these meshes consist of 1654 elements and 1777 nodes.

Since it is interesting to evaluate the performance of the proposed procedure compared to other existing procedures, an additional finite element model has been created, in which the gear geometries have been meshed using the Argyris [15] procedure (denoted as **Comparison** model). This well-known meshing procedure produces a uniform quadrilateral structured mesh over the gear geometries, as the one shown in Fig. 12b. This mesh has been developed trying

to minimize the distortion of the elements of the mesh, with the constraint that its number of nodes and elements must be in the same order of magnitude than in the mesh generated with the proposed procedure (Fig. 12a).

Regarding the computational cost, the generation of the mesh for both gears in the **Proposed** model (Fig. 12a) took less than 2 seconds, where 22.4% of the time was spent generating the mesh itself (first part) and the other 77.6% of the time was spent optimizing the mesh (second part). On the other hand, the generation of the mesh of the **Comparison** model (Fig. 12b) took less than 0.3 seconds, a time of the same order of magnitude than the one associated to the first part of the proposed approach.

Beyond the obvious differences that are revealed by a visual comparison between both meshes, a more exhaustive comparison can be established in terms of the distortion of their elements, measured using Oddy's mesh quality metric [39]. For such a purpose, Fig. 13 shows a contour plot of the element distortion over the drive gear of both models. In this figure the amount of element distortion is indicated using a grayscale code, where the elements become darker as their distortion increases.

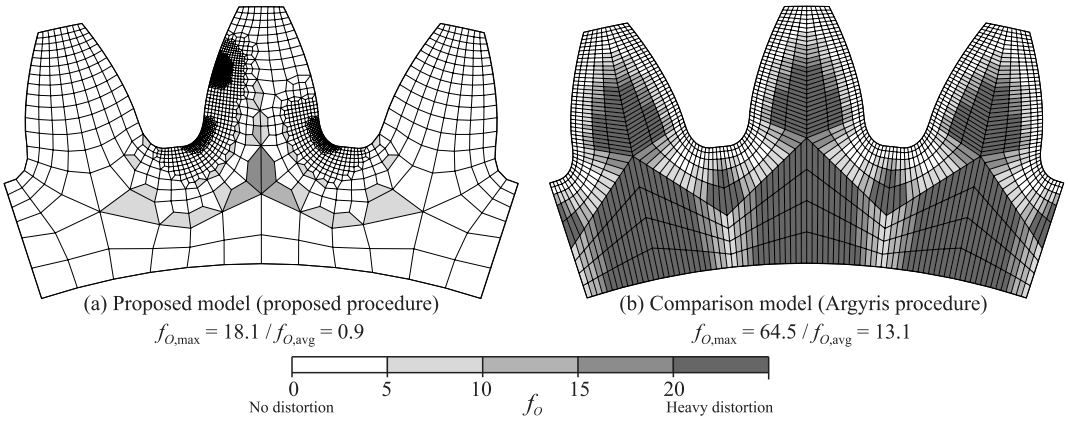

Figure 13: Distortion metrics for the meshes generated using the proposed and Argyris' procedures

As it can be observed in Fig. 13a, the proposed procedure tends to generate distorted elements in the areas where a transition from a coarse to a fine mesh is produced. Besides these transition elements, no distorted elements can be found inside of the refinement areas. On the other hand, Fig. 13b shows that Argyris procedure may be capable to produce undistorted elements in the external layers of the mesh, but elements with severe distortion are generated in the central part of the gear teeth.

The maximum element distortion ($f_{O,max}$) in the mesh generated using Argyris' procedure is 3 times greater than in the mesh generated using the proposed procedure, and the average element distortion ($f_{O,avg}$) is 13 times higher in the mesh generated by Argyris' procedure than in the mesh generated using the proposed procedure. These values indicate that the proposed procedure generates

meshes with less distortion than Argyris' procedure.

To assess the performance of these meshes, both finite element models are analyzed and the accuracy of the obtained results is evaluated. This comparison requires of some reference results, which are obtained using a third finite element model (denoted by **Reference** model), in which the gear geometries are meshed using an extremely refined uniform mesh. These meshes are created using the procedure described in section 2, considering the seeding scheme proposed in section 3.3 with $n_{seg} = 32$. As a result, each gear geometry is discretized into 105795 nodes and 104448 elements.

Note that the **Reference** model is about 100 times larger (in terms of number of nodes and elements) than the **Proposed** model, so its associated computational cost is increased. The **Reference** model is not shown because the finite element mesh is so dense that results in a black-filled figure. However, certain parts of this mesh are shown in Fig. 15a and Fig. 16a.

Abaqus FEA solver [42] was used to perform a static analysis of the three finite element models. For such a a purpose, element type CPE4 was assigned to the elements of the mesh, which is a plane strain 4-node bilinear element with selectively reduced integration. Abaqus solved the **Proposed** and **Comparison** models in less than 6 seconds, but it needed 228 seconds to solve the **Reference** model.

Figure 14a shows the contact pressure distribution that arises as a consequence of the contact between the gear teeth. In this figure, each point represents the contact pressure associated to a node of the drive gear contact profile. The figure also shows the theoretical solution predicted by the Hertz contact theory [43, 44], which consists in a semielliptic function characterized by the maximum contact pressure and the width of the contact area.

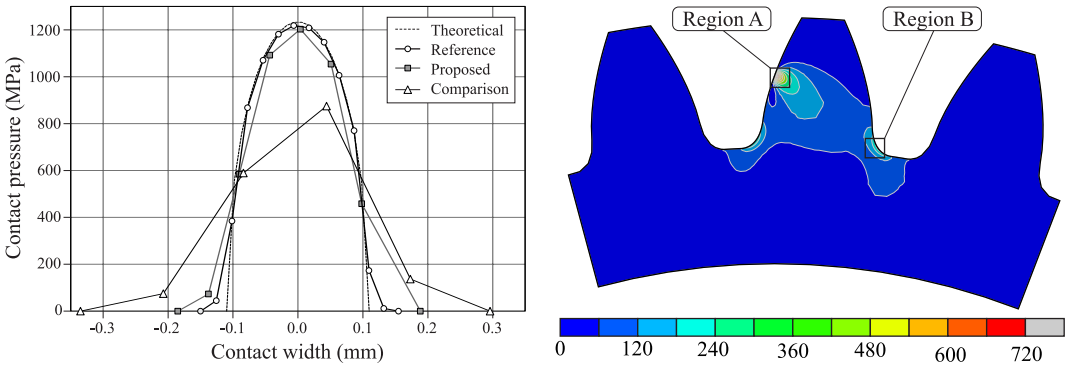

(a) Contact pressure distribution

(b) Von Mises stress plot (values in MPa)

Figure 14: Relevant results of the finite element analyses

The maximum contact pressure and the width of the contact area obtained from each one of the studied models are summarized in Tab. 4. Judging the results shown in Fig. 14a and Tab. 4, it can be said that the best approximation to the theoretical solution (in terms of contact pressure distribution, maximum

Table 4: Relevant contact results

Contact parameters	Hertz	Reference	Proposed	Comparison
Avg. element size	–	0.023 mm	0.047 mm	0.126 mm
Max. contact pressure	1233 MPa	1218 MPa	1203 MPa	875 MPa
Width of the contat area	0.22 mm	0.30 mm	0.37 mm	0.63 mm

contact pressure and width of the contact area) is achieved using the **Reference** model. On the contrary, the worst approximation is obtained from the **Comparison** model, where the maximum contact pressure is 29% lower than the theoretical result. The **Proposed** model represents a slightly worse approximation than the **Reference** model, but its accuracy is significantly better than the **Comparison** model.

Table 4 also summarizes the average size of the elements within the contact area, having the **Reference** model the smallest elements and the **Comparison** model the largest ones. It can be observed that there exists an explicit relation between the size of the elements in the the contact area and the accuracy of the obtained results, which evidences the importance of having a refined mesh in the vicinity of the contact area.

On the other hand, Fig. 14b shows the von Mises stress plot over the geometry of the drive gear, which is obtained using the **Proposed** model. As expected, the maximum von Mises stress is produced in the vicinity of the contact area and, in addition, elevated von Mises stresses are produced at the fillet regions. The regions where these stresses reach their maximum values are shown in greater detail in Fig. 15b and Fig. 16b.

Figure 15a shows the von Mises stress plot obtained from the **Reference** model for the area denoted as *Region A* in Fig. 14b. The small size of the elements in which the gear geometries of this model have been discretized allows for a proper representation of the stress field. The von Mises contact stress reaches a maximum value of 753.4 MPa at a certain distance below the contact surface, which is in good agreement with the theoretical solutions included in Ref. [33].

The von Mises stress plot obtained using the **Proposed** model is shown in Fig. 15b. Although the level of mesh refinement at this part of the mesh is coarser than in the **Reference** model, this model is still capable of representing accurately the stress field in this area (including a realistic location of the maximum stress point under the tooth surface), with a deviation lower than 2% respect to the maximum stress value predicted by the **Reference** model. This deviation is much larger in the results obtained from the **Comparison** model, which is shown in Fig. 15c. In this case, the maximum contact stress is almost a 15% lower than in the **Reference** model, and the stress field presents important differences with the one obtained from the **Reference** model. As an example, this model predicts that the maximum stress point is on the tooth

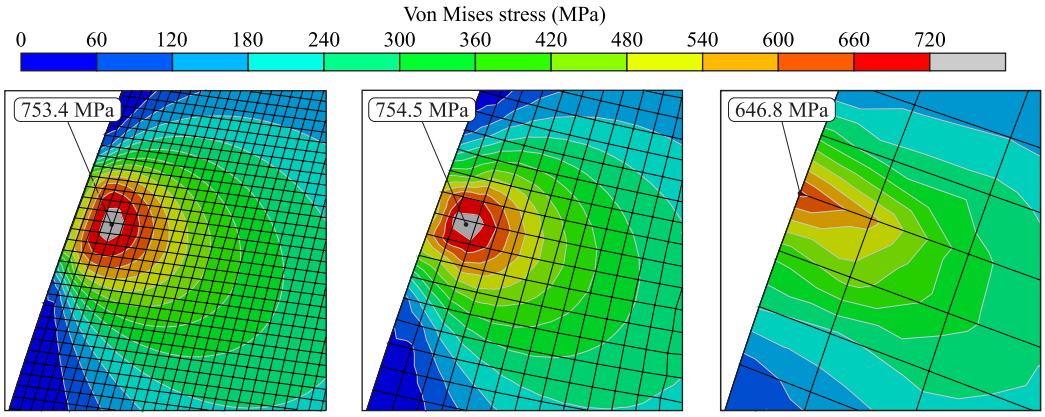

(a) Reference model (b) Proposed model (c) Comparison model

Figure 15: Von Mises contact stress in region A

surface, which is not realistic.

Regarding the bending stresses, Fig. 16a shows the von Mises stress plot obtained from the **Reference** model for the area denoted as *Region B* in Fig. 14b. As it can be observed, the maximum von Mises stress in this area reaches 259.5 MPa and it is located at the fillet surface. In the case of the **Proposed** model, whose result is shown in Fig. 14b, a deviation lower than 3% is obtained in comparison with the **Reference** model. Finally, and following the trend observed in the contact stresses, the maximum von Mises stress calculated using the **Comparison** model is 12% lower than the reference results.

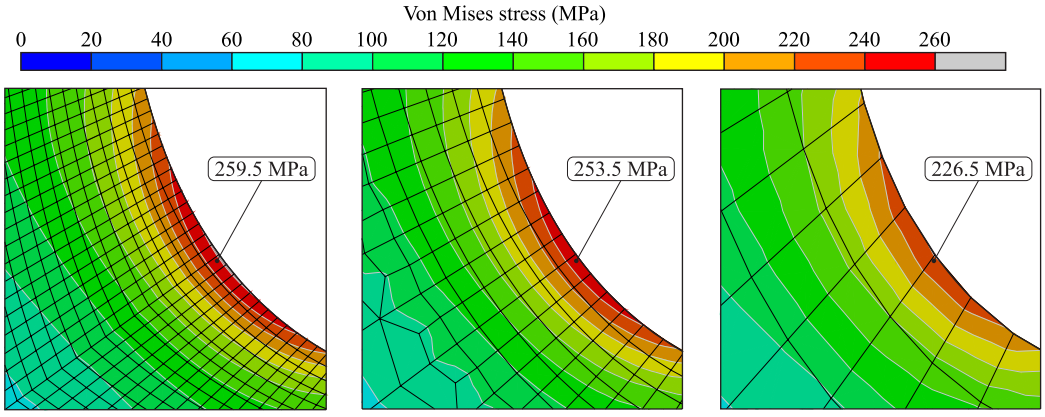

(a) Reference model (b) Proposed model (c) Comparison model

Figure 16: Von Mises bending stress at the right fillet of the tooth (region B)

As a summary of this comparison, it can be said that the finite element model developed using the proposed procedure (**Proposed** model) is capable

of obtaining results with the degree of accuracy of the **Reference** model, but at a much lower computational cost. This comparison has also revealed that the results obtained from the **Proposed** model are more accurate than the results obtained from the **Comparison** model, having both of them a similar associated computational cost. In fact, it has been observed that the **Comparison** model tends to underestimate both the maximum contact pressure and bending stress, and this could compromise the integrity of the transmission designed using these results.

The previous example demonstrates the performance of the proposed procedure when studying a situation in which the contact is produced between a single pair of teeth. But this procedure can also be used to develop meshes in situations where a multi-tooth contact is produced, as it is illustrated in Fig. 17. In this case, the fillets and the contact profiles of the two teeth bearing the load are refined. In Fig. 17a, the refinement parameters shown in Tab. 3 have been used, whereas in Fig. 17b one level of refinement has been decreased in all the refinement areas.

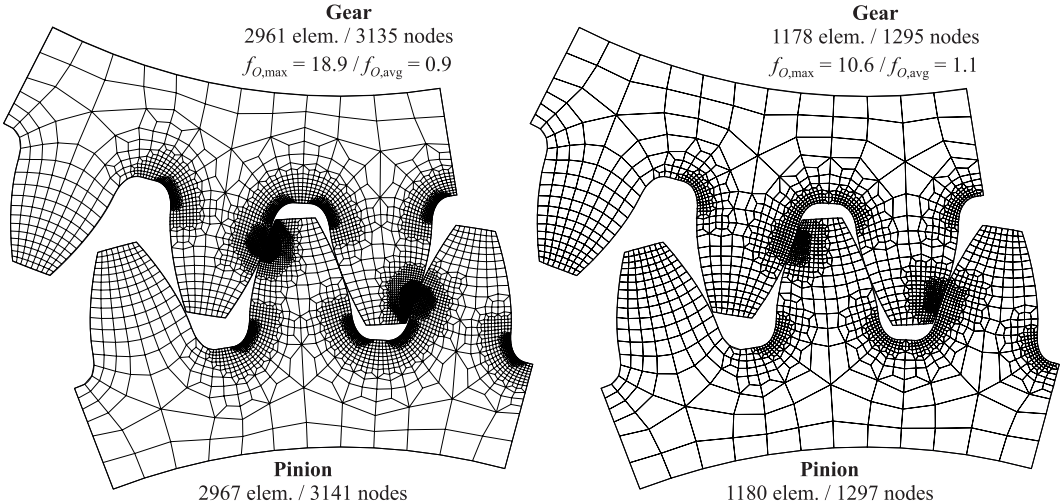

Figure 17: Multi-tooth contact

Comparing the meshes shown in Fig. 17a and Fig. 13a, it can be observed that the addition of more refinement areas does not have a significant negative repercussion over the distortion metrics of the mesh. Note that, since the mesh refinement is based on the subdivisions of the elements of the base mesh, and the elements of the base mesh are smaller near the tip of the tooth than in the root, refined elements with the same level of refinement are also smaller in the tip than in the root. On the other hand, the comparison between the meshes shown in Fig. 17a and Fig. 17b shows that reducing the level of refinement also

reduces the distortion of the elements of the mesh, since a minor number of transition elements are required.

6. Conclusions

In this work a new meshing procedure for automated generation of two-dimensional quadrilateral meshes of gear drives is proposed. The procedure is developed to enable the performance of fully controlled local mesh refinement, as it is an important feature to increase the accuracy of the results of the analyses and reduce its computational cost. It consists of two sequential steps: in the first step, a base quadrilateral mesh is generated using a multiblock meshing scheme and, in the second step, the elements of the base mesh are subdivided to achieve a refined mesh in specific areas of the gear teeth.

To improve the quality of the resulting meshes, the proposed procedure is completed with a mesh quality enhancement technique, which consists in an optimization-based smoothing. The proposed procedure also includes strategies that allow to automatically identify and refine those areas of the gear where elevated mesh densities are usually required (as they are subjected to elevated stress gradients).

The performance of the proposed procedure has been illustrated with numerical examples consisting in the development and analysis of a finite element model of a spur gear transmission. The obtained mesh has been compared to a traditional meshing procedure, demonstrating high capabilities in terms of mesh quality and accuracy of the obtained results.

Future work on this topic can be directed towards adapting the proposed procedure to mesh three dimensional gear geometries. The same steps followed in this work (i.e. generation of a base hexahedral mesh, performance of mesh refinement using three dimensional refinement templates and optimization of the generated mesh) could be followed for such a purpose. However, further investigations should be made to extend the used methods to the three dimensional case, ensure their robustness and guarantee the quality of the resulting mesh.

Acknowledgements

The authors express their deep gratitude to the Universitat Jaume I for the financial support of research project ref. UJI-A2019-024.

References

[1] L. Wilcox, W. Coleman, Application of Finite Elements to the Analysis of Gear Tooth Stresses, Journal of Engineering for Industry 95 (4) (1973) 1139–1148. doi:10.1115/1.3438262.

[2] K. Mao, Gear tooth contact analysis and its application in the reduction of fatigue wear, Wear 262 (5-6) (2007) 505–513. doi:10.1016/j.wear.2006.08.027.

[3] S. Patil, S. Karuppanan, I. Atanasovska, A. Wahab, Contact stress analysis of helical gear pairs, including frictional coefficients, International Journal of Mechanical Sciences 85 (2014) 205–211. doi:10.1016/j.ijmecsci.2014.05.013.

[4] M. Hotait, A. Kahraman, T. Nishino, An investigation of root stresses of hypoid gears with misalignments, Journal of Mechanical Design, Transactions of the ASME 133 (7) (2011). doi:10.1115/1.4004224.

[5] C. Hasl, H. Liu, P. Oster, T. Tobie, K. Stahl, F. fuer Zahnraeder und Getriebebau (Gear Research Centre), Method for calculating the tooth root stress of plastic spur gears meshing with steel gears under consideration of deflection-induced load sharing, Mechanism and Machine Theory 111 (2017) 152–163. doi:10.1016/j.mechmachtheory.2017.01.015.

[6] V. Roda-Casanova, F. Sanchez-Marin, A 2d finite element based approach to predict the temperature field in polymer spur gear transmissions, Mechanism and Machine Theory 133 (2019) 195–210. doi:10.1016/j.mechmachtheory.2018.11.019.

[7] C. Fernandes, D. Rocha, R. Martins, L. Magalhães, J. Seabra, Finite element method model to predict bulk and flash temperatures on polymer gears, Tribology International 120 (2018) 255–268. doi:10.1016/j.triboint.2017.12.027.

[8] B. Černe, M. Petkovšek, J. Duhovnik, J. Tavčar, Thermo-mechanical modeling of polymer spur gears with experimental validation using high-speed infrared thermography, Mechanism and Machine Theory 146 (2020). doi:10.1016/j.mechmachtheory.2019.103734.

[9] F. L. Litvin, A. Fuentes, Gear Geometry and Applied Theory, 2nd Edition, Cambridge University Press, 2004. doi:10.1017/CBO9780511547126.

[10] J. Coy, D. Townsend, E. Zaretsky, Gearing, Tech. rep., NASA Lewis Research Center (1985).

[11] N. Lee, K. Bathe, Effects of element distortions on the performance of isoparametric elements, International Journal for Numerical Methods in Engineering 36 (20) (1993) 3553–3576. doi:10.1002/nme.1620362009.

[12] J. R. Shewchuk, What is a good linear finite element? - interpolation, conditioning, anisotropy, and quality measures, Tech. rep., In Proc. of the 11th International Meshing Roundtable (2002).

[13] P. M. Knupp, Remarks on mesh quality, in: 45th AIAA Aerospace Sciences Meeting and Exhibit, 7-10 January, 2007, Reno, NV, 2007.

[14] J. Coy, C. Chao, A method of selecting grid size to account for hertz deformation in finite element analysis of spur gears., Journal of Mechanical Design 104 (1982). doi:10.1115/1.3256429.

[15] J. Argyris, A. Fuentes, F. Litvin, Computerized integrated approach for design and stress analysis of spiral bevel gears, Computer Methods in Applied Mechanics and Engineering 191 (11-12) (2002) 1057–1095. doi:10.1016/S0045-7825(01)00316-4.

[16] J. Pedrero, M. Pleguezuelos, M. Artés, J. Antona, Load distribution model along the line of contact for involute external gears, Mechanism and Machine Theory 45 (5) (2010) 780–794. doi:10.1016/j.mechmachtheory.2009.12.009.

[17] C. Zanzi, J. Pedrero, Application of modified geometry of face gear drive, Computer Methods in Applied Mechanics and Engineering 194 (27-29) (2005) 3047–3066. doi:10.1016/j.cma.2004.07.022.

[18] N. Cappellini, T. Tamarozzi, B. Blockmans, J. Fiszer, F. Cosco, W. Desmet, Semi-analytic contact technique in a non-linear parametric model order reduction method for gear simulations, Meccanica 53 (1-2) (2018) 49–75. doi:10.1007/s11012-017-0710-5.

[19] S. Li, Finite element analyses for contact strength and bending strength of a pair of spur gears with machining errors, assembly errors and tooth modifications, Mechanism and Machine Theory 42 (1) (2007) 88 – 114. doi:https://doi.org/10.1016/j.mechmachtheory.2006.01.009.

[20] I. Gonzalez-Perez, J. L. Iserte, A. Fuentes, Implementation of hertz theory and validation of a finite element model for stress analysis of gear drives with localized bearing contact, Mechanism and Machine Theory 46 (6) (2011) 765 – 783. doi:https://doi.org/10.1016/j.mechmachtheory.2011.01.014.

[21] M. Barbieri, A. Zippo, F. Pellicano, Adaptive grid-size finite element modeling of helical gear pairs, Mechanism and Machine Theory 82 (2014) 17 – 32. doi:https://doi.org/10.1016/j.mechmachtheory.2014.07.009.

[22] I. Gonzalez-Perez, A. Fuentes-Aznar, Implementation of a finite element model for stress analysis of gear drives based on multi-point constraints, Mechanism and Machine Theory 117 (2017) 35–47. doi:10.1016/j.mechmachtheory.2017.07.005.

[23] I. Gonzalez-Perez, A. Fuentes-Aznar, Implementation of a finite element model for gear stress analysis based on tie-surface constraints and its validation through the hertz's theory, Journal of Mechanical Design, Transactions of the ASME 140 (2) (2018). doi:10.1115/1.4038301.

[24] C. Roarty, N. Grosland, Adaptive meshing technique applied to an orthopaedic finite element contact problem., The Iowa orthopaedic journal 24 (2004) 21–29.

[25] A. Keskin, M. Kober, E. Stelldinger, A. Kühhorn, H. Böhm, A. Hornig, A. Langkamp, M. Gude, On the quantification of errors of a preprocessing effort reducing contact meshing approach, 2015. doi:10.2514/6.2015-0408.

[26] V. Roda-Casanova, F. Sanchez-Marin, Development of a multiblock procedure for automated generation of two-dimensional quadrilateral meshes of gear drives, Mechanism and Machine Theory 143 (2020). doi:https://doi.org/10.1016/j.mechmachtheory.2019.103631.

[27] P. Frey, P. George, Mesh generation applied to finite elements, Hermes Science, 2000.

[28] M. Farrashkhalvat, J. Miles, Basic Structured Grid Generation: With an introduction to unstructured grid generation, Elsevier Science, 2003.

[29] H. L. Nguyen, On the applications of algebraic grid generation methods based on transfinite interpolation, Tech. rep., NASA Lewis Research Center (1989).

[30] W. Gordon, C. Hall, Construction of curvilinear co-ordinate systems and applications to mesh generation, International Journal for Numerical Methods in Engineering 7 (4) (1973) 461–477. doi:10.1002/nme.1620070405.

[31] V. Roda-Casanova, F. Sanchez-Marin, An adaptive mesh refinement approach for solving non-hertzian elastic contact problems, Meccanica 53 (8) (2018) 2013–2028. doi:10.1007/s11012-017-0806-y.

[32] R. Schneiders, Refining quadrilateral and hexahedral element meshes, in: 5th International Conference on Grid Generation in Computational Field Simulations, CRC Press, 1996, pp. 679–688.

[33] G. Hamilton, L. Goodman, The stress field created by a circular sliding contact, Journal of Applied Mechanics, Transactions ASME 33 (2) (1964) 371–376. doi:10.1115/1.3625051.

[34] ISO/FDIS 6336-3, Calculation of load capacity of spur and helical gears. Part 3: calculation of tooth bending strength, Tech. rep., International Organization for Standarization, Geneva, Switzerland (2006).

[35] R. Cook, Finite Element Modeling for Stress Analysis, John Wiley and Sons, Inc., 1995.

[36] S. A. Canann, J. R. Tristano, M. L. Staten, An approach to combined laplacian and optimization-based smoothing for triangular, quadrilateral, and quad-dominant meshes, in: 7th International Meshing Roundtable, 1998.

[37] J. Park, S. M. Shontz, An alternating mesh quality metric scheme for efficient mesh quality improvement, Procedia Computer Science 4 (2011) 292 – 301, proceedings of the International Conference on Computational Science, ICCS 2011. doi:10.1016/j.procs.2011.04.031.

[38] W. Buell, B. Bush, Mesh generation–a survey, Journal of Manufacturing Science and Engineering, Transactions of the ASME 95 (1) (1973) 332–338.

[39] A. Oddy, J. Goldak, M. McDill, M. Bibby, Distortion metric for isoparametric finite elements, Transactions of the Canadian Society for Mechanical Engineering 12 (4) (1988) 213–217.

[40] P. M. Knupp, Achieving finite element mesh quality via optimization of the jacobian matrix norm and associated quantities. part i—a framework for surface mesh optimization, International Journal for Numerical Methods in Engineering 48 (3) (2000) 401–420. doi:10.1002/(SICI)1097-0207(20000530)48:3<401::AID-NME880>3.0.CO;2-D.

[41] S. Canann, M. Stephenson, T. Blacker, Optismoothing: An optimization-driven approach to mesh smoothing, Finite Elements in Analysis and Design 13 (2-3) (1993) 185–190. doi:10.1016/0168-874X(93)90056-V.

[42] Abaqus Theory Guide, Dassault Systèmes Simulia Corp, United States, 2015.

[43] K. L. Johnson, Contact Mechanics, Cambridge University Press, 1985. doi:10.1017/CBO9781139171731.

[44] ISO/FDIS 6336-2, Calculation of load capacity of spur and helical gears. Part 2: Calculation of surface durability, Tech. rep., International Organization for Standarization, Geneva, Switzerland (2006).